

RESEARCH ARTICLE

Electrochemical and microstructural characterization of the high-entropy perovskite $\text{La}_{0.2}\text{Pr}_{0.2}\text{Nd}_{0.2}\text{Sm}_{0.2}\text{Sr}_{0.2}\text{CoO}_{3-\delta}$ for solid oxide cell air electrodes

Patrick Pretschuh¹  | Andreas Egger¹  | Roland Brunner² | Edith Bucher¹ 

¹Department General, Analytical and Physical Chemistry, Montanuniversitaet Leoben, Chair of Physical Chemistry, Leoben, Austria

²Department Microelectronics, Materials Center Leoben Forschung GmbH, Leoben, Austria

Correspondence

Edith Bucher, Montanuniversitaet Leoben, Chair of Physical Chemistry, Franz-Josef-Straße 18, AT-8700 Leoben, Austria.

Email: edith.bucher@unileoben.ac.at

Funding information

Zukunftsfonds Steiermark, Grant/Award Number: 1704

Abstract

Strontium segregation (coupled to phase decomposition and impurity poisoning) and electrode delamination are two of the most important degradation mechanisms currently limiting the long-term stability of solid oxide fuel cell and electrolysis cell (SOFC and SOEC) air electrodes. The present study aims to demonstrate that air electrodes made of entropy-stabilized multi-component oxides can mitigate these degradation mechanisms while providing excellent cell performance. A SOEC utilizing $\text{La}_{0.2}\text{Pr}_{0.2}\text{Nd}_{0.2}\text{Sm}_{0.2}\text{Sr}_{0.2}\text{CoO}_{3-\delta}$ (LPNSSC) as an air electrode delivers -1.56 A/cm^2 at 1.2 V at 800°C. This performance exceeds that of a commercial cell with $\text{La}_{0.6}\text{Sr}_{0.4}\text{CoO}_{3-\delta}$ (LSC) air electrode, which reaches -1.43 A/cm^2 . In a long-term electrolysis test, the LPNSSC cell shows stable performance during 700 h, while the LSC cell degrades continuously. Post-mortem analyses by scanning electron microscopy-energy dispersive X-ray spectroscopy indicate complete delamination of the LSC electrode, while LPNSSC shows excellent adhesion. The amount of secondary phases formed (esp. SrSO_4) is also much lower in LPNSSC compared to LSC. In conclusion, the high-entropy perovskite LPNSSC is a promising option for air electrodes of solid oxide cells. While LPNSSC can compete with – or even outperform – LSC air electrodes in terms of electrochemical performance, it could be particularly advantageous in terms of long-term stability in SOEC mode.

KEYWORDS

electrochemical characterization, fuel cell electrode, high-entropy perovskite, microstructural characterization, solid oxide electrolysis cell, solid oxide fuel cell, strontium segregation

1 | INTRODUCTION

Nowadays, hydrogen is acknowledged as a fundamental component of a sustainable green industry [1–3] and potential fields of application include many energy-intensive industrial divisions [4–6]. In addition to efficient storage

and transport, one of the biggest hurdles is the sustainable production of green hydrogen. In this context, high-temperature water electrolysis with solid oxide cells (SOCs) is a promising technology for large-scale applications [7, 8]. Moreover, solid oxide fuel cells (SOFCs), solid oxide electrolysis cells (SOECs), or reversible SOCs

This is an open access article under the terms of the [Creative Commons Attribution-NonCommercial](https://creativecommons.org/licenses/by-nc/4.0/) License, which permits use, distribution and reproduction in any medium, provided the original work is properly cited and is not used for commercial purposes.

© 2023 The Authors. Fuel Cells published by Wiley-VCH GmbH.

(RSOCs) can also be applied as power balancing or independent power supply systems [9]. Such industrial-scale plants can play an important role in buffering fluctuating and seasonal wind and solar energy [10]. Especially in combination with applications that also require or supply thermal energy, SOCs can develop their full potential [11]. Although application areas are growing, there are still some challenges for SOCs to achieve broad market penetration. These issues concern in particular the costs of materials and systems, which go hand in hand with the efficiency and lifetime of SOC solutions. The air electrode is a key component of SOCs [12], which requires materials with excellent electrochemical performance and good long-term stability [13–16]. Especially in the electrolysis mode, delamination of the air electrode is a critical degradation mechanism caused by high internal oxygen pressure in the electrolyte close to the air electrode interface [17]. In addition, Sr segregation is one of the main reasons for air electrode degradation in state-of-the-art (SOTA) perovskites like $\text{La}_{0.6}\text{Sr}_{0.4}\text{Co}_{0.2}\text{Fe}_{0.8}\text{O}_{3-\delta}$ (LSCF) [18–21] and $\text{La}_{0.6}\text{Sr}_{0.4}\text{CoO}_{3-\delta}$ (LSC) [22–26]. High-entropy (multi-component) oxides are a relatively new strategy to stabilize ceramic compounds through their increased configurational entropy [27]. This approach is also suitable to improve the thermodynamic stability of perovskites (general formula ABO_3) by mixing $n \geq 5$ cations on the A- and/or B-sites of the crystal lattice [27–30]. Compared to low-entropy perovskites (LEP) such as LSCF, Sr segregation is suppressed in medium- (MEP) and high-entropy perovskites (HEP) [31, 32]. Good electrochemical performances and low polarization resistances are reported for SOCs with HEP and MEP air electrodes [31–34]. However, there is a need for further experimental verification and deeper insights into the structure-property relationships in order to prove enhanced long-term stability of electrochemical SOCs with HEP electrodes. In the present study, the HEP $\text{La}_{0.2}\text{Pr}_{0.2}\text{Nd}_{0.2}\text{Sm}_{0.2}\text{Sr}_{0.2}\text{CoO}_{3-\delta}$ (LPNSSC) is characterized as a SOC air electrode in terms of electrochemical performance, long-term stability, microstructure, and cation distribution. The composition LPNSSC was selected in analogy to the well-investigated low-entropy perovskites from the series $(\text{La,Sr})\text{CoO}_{3-\delta}$, which show high electronic and significant ionic conductivities and fast oxygen exchange kinetics [35, 36], but limited long-term stability [37, 38]. For the A-site, Pr, Nd, and Sm were chosen in addition to La and Sr since these rare earth elements have similar ionic radii as La and Sr [39]. In order to maximize the configurational entropy (Equation S1), the five cations were used in equimolar amounts of 0.2 each. In particular, this work aims at demonstrating that the power densities and long-term stabilities of cells with HEP electrodes can exceed those of cells with SOTA perovskites, especially in SOEC mode, and that Sr segregation

and delamination of the air electrode are lower for HEPs compared to SOTA electrode materials.

2 | EXPERIMENTAL SECTION

2.1 | Synthesis of LPNSSC

LPNSSC powder is synthesized by the citric acid–ethylenediaminetetraacetate (CA-EDTA) sol-gel method. Stoichiometric amounts of metal nitrates, that is, $\text{La}(\text{NO}_3)_3 \cdot 6\text{H}_2\text{O}$, $\text{Pr}(\text{NO}_3)_3 \cdot 6\text{H}_2\text{O}$, $\text{Nd}(\text{NO}_3)_3 \cdot 6\text{H}_2\text{O}$, $\text{Sm}(\text{NO}_3)_3 \cdot 6\text{H}_2\text{O}$, $\text{Sr}(\text{NO}_3)_2$ and $\text{Co}(\text{NO}_3)_2 \cdot 6\text{H}_2\text{O}$ (all chemicals purchased from Aldrich, purity $\geq 99.0\%$), are dissolved in deionized water, stirred, heated and mixed with 1 mol anhydrous citric acid per mol of cations. A pH of 8 is adjusted by the addition of an aqueous ammonia solution. The temperature of the solution is then raised on a hot plate to evaporate water and form a gel. After the water is completely evaporated, spontaneous combustion occurs, and the temperature is maintained until the gel is completely converted to raw ash. The powder is homogenized with an agate mortar and then calcined for 4 h at 1000°C in the air with heating and cooling rates of 5 K/min^1 .

2.2 | Preparation of cells

The calcined LPNSSC powder is milled for 48 h on a rolling bench using 3 mm diameter zirconia balls in ethanol until a particle size distribution with d_{50} of approximately $0.5\ \mu\text{m}$ is reached. A terpeneol-based ink vehicle containing 6 wt.% ethyl cellulose is used to produce a screen-printing paste containing 66 wt.% LPNSSC. The paste is screen-printed onto commercially available 2 cm diameter round anode-supported cell (ASC) substrates (fuelcellmaterials) and $5 \times 5\ \text{cm}^2$ square ASC substrates (Elcogen AS). The active area of the cells is $1.1\ \text{cm}^2$ (button cells) and $16\ \text{cm}^2$ (square cells). The cells with the printed electrodes are sintered for 2 h at 1070°C with heating rates of 5 K/min and cooling rates of 2 K/min . A commercial $5 \times 5\ \text{cm}^2$ ASC consisting of an LSC air electrode, GDC diffusion barrier, YSZ electrolyte, and Ni-YSZ fuel electrode (Elcogen AS) was used as a benchmark for comparison with the $5 \times 5\ \text{cm}^2$ LPNSSC cell.

2.3 | Microstructural characterization

The microstructure of the cells is investigated by field emission scanning electron microscopy (FESEM) using a ZEISS 450 GeminiSEM in backscattered electron (BSE)

and secondary electron (SE) mode with 5 kV and 3 nA. For the preparation of specimen cross sections, the cells are sectioned with a diamond wire saw and then cut with a Hitachi IM400Plus ion slicer. A thin layer of gold is sputtered onto the samples to ensure good electrical conductivity. The distribution of chemical elements is mapped by energy dispersive X-ray spectroscopy (EDX) using an Ultim Extreme detector from Oxford Instruments at an energy range of 10 keV.

2.4 | Electrochemical characterization

Button cells with a diameter of 2 cm are investigated using a Probostat system (NorECs Norwegian Electro Ceramics AS) and a frequency response analyzer (Novocontrol Alpha-A) with potentiostat/galvanostat interface (Novocontrol POT/GAL 15 V/10 A). Electrochemical impedance spectroscopy (EIS) is performed in a four-wire configuration in the frequency range of 10 mHz – 1 MHz. The cells are placed in an alumina sample holder inside a tubular furnace. Gold sealant ensures gas tightness between the air side and the fuel side. Ni-mesh/Ni-paste and Pt-mesh/Pt-paste are used for current collection on the fuel electrode and air electrode, respectively.

Square $5 \times 5 \text{ cm}^2$ cells are electrochemically characterized with an Evaluator C50-HT (Horiba FuelCon GmbH) system. The cells are placed between an alumina plate and a polished ceramic cell housing to ensure gas tightness. Ni- and Pt-meshes (without metallic contact pastes) are used as current collectors on the fuel and air electrode sides, respectively. A mechanical load of 1 kg is used to improve the gas tightness and reduce contact resistance.

For both button cells and square cells, the current density-voltage characteristics are recorded at current ramps of up to $3 \text{ mA}/(\text{cm}^2 \text{ s})$ until the voltage reaches at least 1.2 V (SOEC) or drops to 0.7 V (SOFC). For button cells, the cell performance under continuous load is evaluated at a gas flow of 40 ml/min at the fuel electrode and 100 ml/min at the air electrode. For SOEC operation, the fuel stream is humidified with a Humistat setup (NorECs Norwegian Electro Ceramics AS). For the $5 \times 5 \text{ cm}^2$ planar cells, the fuel and air flow rates are 1 l/min unless otherwise specified. Heating and cooling rates are 2 K/min for button cells and 1 K/min for $5 \times 5 \text{ cm}^2$ ASCs.

3 | RESULTS AND DISCUSSION

3.1 | Electrochemical characterization

The performance of LPNSSC | GDC | YSZ | Ni-YSZ button cells is evaluated in SOFC mode in the temperature

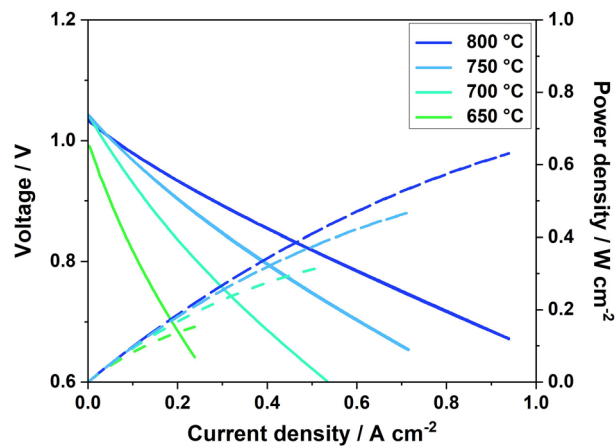


FIGURE 1 Current-voltage curves (solid lines) and power densities (dashed lines) of a button cell with $\text{La}_{0.2}\text{Pr}_{0.2}\text{Nd}_{0.2}\text{Sm}_{0.2}\text{Sr}_{0.2}\text{CoO}_{3-\delta}$ (LPNSSC) air electrode in solid oxide fuel cell (SOFC) mode at different temperatures. Gas flows were 100 ml/min with 20% O_2 (rest Ar) at the air electrode and 40 ml/min H_2 with 3% H_2O at the fuel electrode.

range from 650°C to 800°C . Figure 1 shows the cell voltage and power density versus the current density. The power densities at 0.7 V are 0.59, 0.42, 0.26, and $0.13 \text{ W}/\text{cm}^2$ at 800, 750, 700, and 650°C , respectively. According to the Nernst equation, the theoretical equilibrium potential for a 97% H_2 / 3% H_2O fuel mixture vs. 20% O_2 at 800°C is 1.10 V. However, the measured open circuit voltage (OCV) at 800°C shows only 1.04 V and also remains below the theoretical value at 650°C . This indicates a minor gas leak due to imperfect sealing, but it is not expected to have a significant impact on the characterization.

Impedance spectra of the button cell are recorded at OCV as shown in Figure 2. The overall polarization resistance R_p and the serial resistance R_s are determined by fitting the curves to an equivalent circuit in the configuration $(L_0 + R_s) + R_1 || \text{CPE}_1 + R_2 || \text{CPE}_2 + R_3 || \text{CPE}_3$. Here L_0 is the inductance of the setup, R_s corresponds to the ohmic part of the impedance, and the resistances R_1 , R_2 , and R_3 add up to R_p . Constant phase elements (CPEs) are used to model the capacitive components of the polarization processes. The CPE values are then converted to equivalent capacitances (C_i) using the procedure described by Fleig [40]. The inductance of the setup L_0 and the serial resistance R_s are subtracted from the data sets shown in Figure 2 for better comparability. Values of R_s and R_p are listed in Table 1 as a function of temperature. A comprehensive overview of the inductive, resistive, and capacitive contributions obtained from impedance analysis is given in Table S1.

The long-term performance and degradation behavior of LPNSSC are investigated in SOEC mode using $5 \times 5 \text{ cm}^2$ planar cells. Initial electrochemical characterization

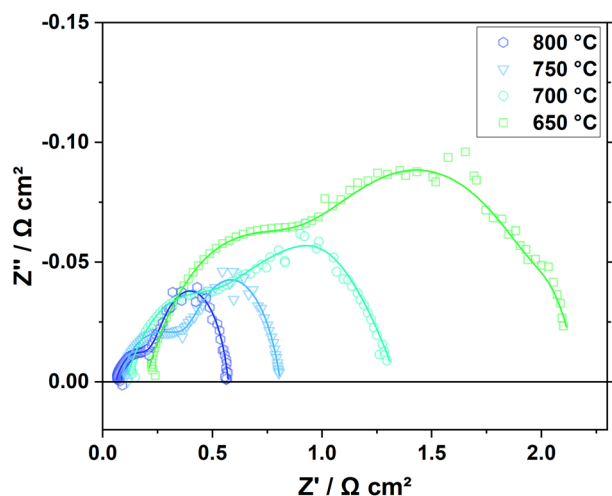


FIGURE 2 Impedance spectra (100 mV below OCV) of the button cell with $\text{La}_{0.2}\text{Pr}_{0.2}\text{Nd}_{0.2}\text{Sm}_{0.2}\text{Sr}_{0.2}\text{CoO}_{3-\delta}$ (LPNSSC) air electrode at different temperatures. Gas flows were 100 ml/min with 20% O_2 (rest Ar) at the air electrode and 40 ml/min H_2 with 3% H_2O at the fuel electrode. Lines are fits with the equivalent circuit described in the text. For better comparability the inductance of the setup and the serial resistance were subtracted from the data sets.

TABLE 1 Serial resistances (R_s) and total polarization resistances (R_p) of the button cell with $\text{La}_{0.2}\text{Pr}_{0.2}\text{Nd}_{0.2}\text{Sm}_{0.2}\text{Sr}_{0.2}\text{CoO}_{3-\delta}$ (LPNSSC) air electrode as obtained from impedance spectra shown in Figure 2.

$T / ^\circ\text{C}$	800	750	700	650
$R_s / \Omega \text{ cm}^2$	0.051	0.066	0.090	0.143
$R_p / \Omega \text{ cm}^2$	0.438	0.626	1.04	1.98

is performed with 90%, 70%, and 50% H_2O (rest H_2). Current densities reach -1.24 , -0.92 , and -0.74 A/cm^2 , respectively, at 1.2 V and 800°C as shown in Figure 3. In addition to the $5 \times 5 \text{ cm}^2$ LPNSSC cell, the electrochemical performance of a 2 cm button cell is investigated in order to evaluate the influence of the different cell sizes and test setups. For the button cell, the SOEC current density at 1.2 V with 70% H_2O is -1.6 A/cm^2 (Figure S1), which is significantly higher than the -0.92 A/cm^2 reached by the $5 \times 5 \text{ cm}^2$ cell (Figure 3). As the layer structure of both cells is very similar, this difference suggests differences in test setups and gas supplies as underlying causes. For example, reducing the $\text{H}_2\text{O}/\text{H}_2$ inlet flow from standard 1 l/min to a lower flow of 0.25 l/min has a significant impact on the electrochemical performance of the $5 \times 5 \text{ cm}^2$ LPNSSC and LSC cells (Figure S4). Taking into account the influencing factors evident in Figure S1, Figure 3, and Figure S4, it is important to note that cell performances should be compared only with identical cell geometries and under identical test conditions, as done in Figure 4.

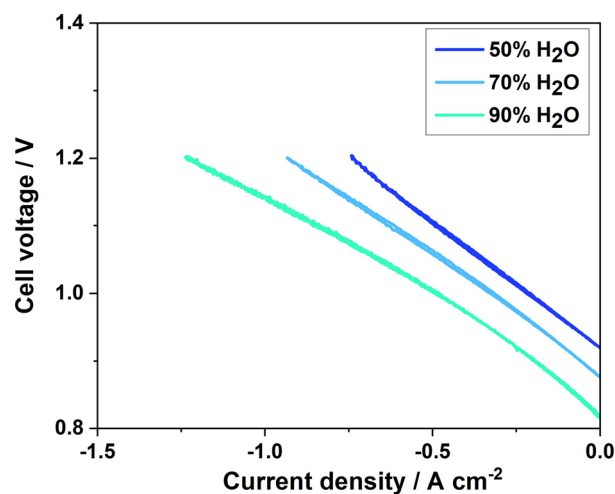


FIGURE 3 Current density-voltage curves of a $5 \times 5 \text{ cm}^2$ cell with $\text{La}_{0.2}\text{Pr}_{0.2}\text{Nd}_{0.2}\text{Sm}_{0.2}\text{Sr}_{0.2}\text{CoO}_{3-\delta}$ (LPNSSC) air electrode at different levels of fuel humidification at 800°C ; gas flows are 1 l/min air at the air electrode and 1 l/min $\text{H}_2/\text{H}_2\text{O}$ at the fuel electrode.

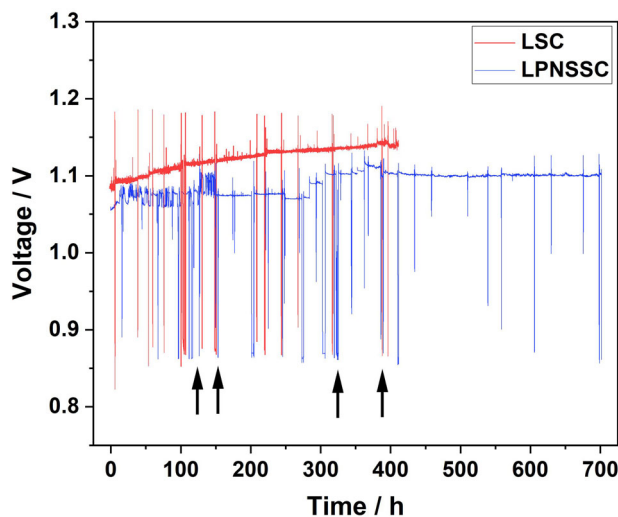


FIGURE 4 Voltage curves of $5 \times 5 \text{ cm}^2$ ASCs with $\text{La}_{0.2}\text{Pr}_{0.2}\text{Nd}_{0.2}\text{Sm}_{0.2}\text{Sr}_{0.2}\text{CoO}_{3-\delta}$ (LPNSSC) (blue) and $\text{La}_{0.6}\text{Sr}_{0.4}\text{CoO}_{3-\delta}$ (LSC) (red) air electrodes during long-term polarization in solid oxide electrolysis cell (SOEC) mode with -0.938 A/cm^2 at 800°C . Arrows mark points in time when uncontrolled shutdowns during the LPNSSC test occurred. Test parameters are 80% H_2O (rest H_2) at the fuel electrode and compressed air at the air electrode, both with 1 l/min gas flow.

Regarding long-term steam electrolysis tests, we compare a commercial anode-supported cell (ASC) with an LSC air electrode (Elcogen AS) with the ASC utilizing the HEP LPNSSC air electrode. Test conditions are the same for both cells and chosen in analogy to published research [41]. Constant current densities of -0.938 A/cm^2 are applied at 800°C during the entire test, while the change of cell voltage is observed, as shown in Figure 4.

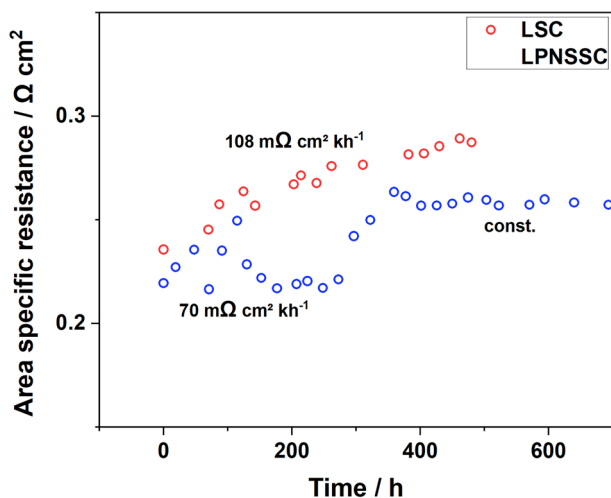


FIGURE 5 ASR of $5 \times 5 \text{ cm}^2$ anode-supported cells (ASCs) with $\text{La}_{0.2}\text{Pr}_{0.2}\text{Nd}_{0.2}\text{Sm}_{0.2}\text{Sr}_{0.2}\text{CoO}_{3-\delta}$ (LPNSSC) and $\text{La}_{0.6}\text{Sr}_{0.4}\text{CoO}_{3-\delta}$ (LSC) air electrodes during long-term solid oxide electrolysis cell (SOEC) studies. Test parameters were 80% humidity (rest H_2) at the fuel electrode and air at the air electrode with 1 l/min gas flow each. A continuous polarization at -0.938 A/cm^2 was applied.

Area-specific resistances (ASRs) are calculated from the average slopes of the current-voltage curves, which are acquired in regular intervals during the long-term measurements (see examples in Figures S2 and S3 for LPNSSC and LSC, respectively). Figure 5 shows the time dependence of the ASR values of the cells with LSC and LPNSSC electrodes. The SOTA cell with an LSC air electrode shows a continuous increase in the cell voltage during SOEC operation for 500 h. The average ASR degradation rate is $108 \text{ m}\Omega \text{ cm}^2$ per 1000 h (estimated by linear interpolation between the measured ASR values at 0 and 450 h), which is similar to degradation rates reported by other groups [42, 43]. In the course of the long-term SOEC test of the cell with LPNSSC air electrode, four thermal cycles were performed due to unintended shutdowns of the test setup (Figure 4). During these shutdowns, heating was turned off and the cell was cooled down to room temperature with undefined cooling rates. Afterwards, the cell was re-heated to 800°C with heating rate of 1 K/min (arrows in Figure 4, cooling/heating ramps not shown). Several step-wise changes of the cell voltage occur (in particular after thermal cycles and recordings of current-voltage curves), which are a consequence of the thermal cycles rather than due to continuous performance degradation. In the first 400 h of testing, where all four thermal cycles occurred, the average increase of the ASR is $70 \text{ m}\Omega \text{ cm}^2$ per 1000 h (estimated by linear interpolation between the measured ASR values at 0 and 400 h) (Figure 5). After stability issues with the test setup were resolved and continuous SOEC operation prevails, no more abrupt changes in cell volt-

age are observed and the voltage of the LPNSSC cell shows virtually no increase in the time interval of 400–700 h (Figure 4). This indicates excellent performance stability of the LPNSSC cell compared to the LSC cell at similar voltage levels.

3.2 | Microstructural characterization of fresh and degraded cells

A FESEM-BSE image of the cross-section of a fresh $5 \times 5 \text{ cm}^2$ ASC with LPNSSC air electrode is shown in Figure 6. It should be noted that the fuel electrode of the freshly prepared cell is not reduced and is therefore composed of NiO-YSZ (not Ni-YSZ). The air electrode shows a homogeneous thickness of $14 \mu\text{m}$ ($\pm 0.3 \mu\text{m}$) and uniform microstructure across the entire analyzed region (Figures S5 and S7). Thresholding-based image analysis of the air electrode yields a porosity of 24%. Image analysis was performed using the software ImageJ [44]. Figure 6 depicts the interfaces between the air electrode, the diffusion barrier (GDC), the electrolyte (YSZ), and the functional layer of the fuel electrode (NiO-YSZ). The layers in contact adhere well to each other. The electrolyte is dense and no cracks or open porosity are observed, whereas the GDC barrier is relatively porous (porosity estimated to be 9%). Figure 6 also shows EDX elemental maps of the same region. The Sr- and Zr-maps indicate the formation of small SrZrO_3 grains at the interface between GDC barrier and YSZ electrolyte, which presumably occurs during the sintering process. As reported in the literature, the porosity of the GDC barrier facilitates the formation of SrZrO_3 via cation interdiffusion [45]. SEM-EDX analyses of a fresh $5 \times 5 \text{ cm}^2$ ASC with LSC air electrode are shown in Figure 7 (see also further images in Figures S6 and S8). The thickness of the LSC air electrode is $16 \mu\text{m}$ ($\pm 0.5 \mu\text{m}$) with a porosity of 36%. Again, the electrolyte layer is dense, whereas the GDC barrier is relatively porous (porosity estimated to be 13%) and EDX images show formation of SrZrO_3 at the GDC/YSZ interface of the LSC cell.

It should be noted that the apparent Co-signals in the fuel electrode (Figure 6d), apparent La/Sr-signals in regions other than the air electrode and the electrode/electrolyte interface (Figures 6b,c, and 7b,c), as well as apparent Y-signals in the air electrode (Figures 6f and 7f) are artifacts due to overlapping or small-intensity peaks in the EDX spectra. These artifacts are more pronounced for the LPNSSC cell due to the larger variety and lower contents of rare earth elements as compared to the LSC cell.

Post-mortem microstructural analyses of $5 \times 5 \text{ cm}^2$ LPNSSC and LSC cells are performed after the SOEC long-term tests using FESEM and EDX. Figure 8a shows the

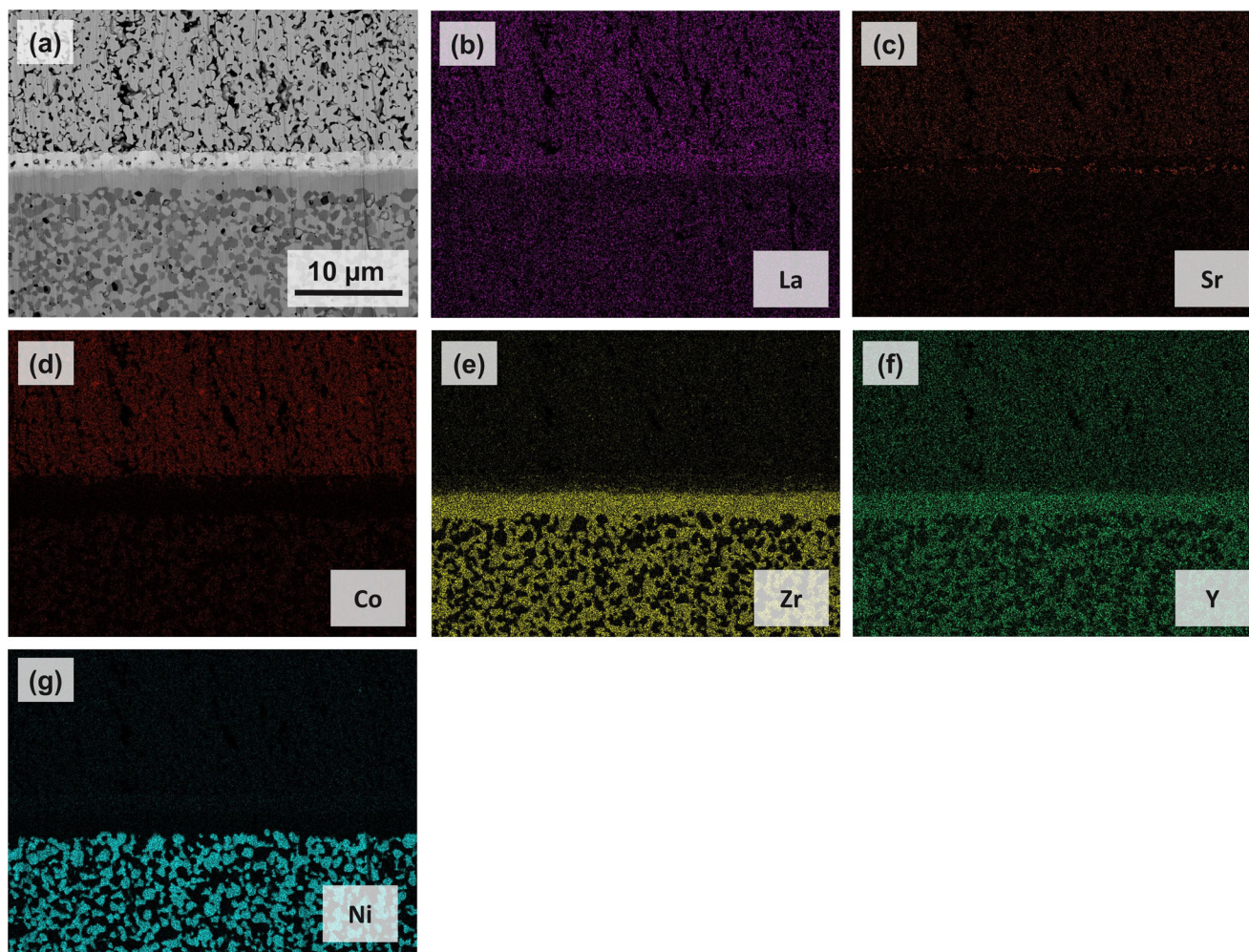


FIGURE 6 Cross-section image of a fresh $5 \times 5 \text{ cm}^2$ anode-supported cell (ASC) with $\text{La}_{0.2}\text{Pr}_{0.2}\text{Nd}_{0.2}\text{Sm}_{0.2}\text{Sr}_{0.2}\text{Co}_{0.3-5}$ (LPNSSC) air electrode recorded by (a) FESEM-BSE; (b–g) elemental maps for La, Sr, Co, Zr, Y, and Ni acquired by energy dispersive X-ray spectroscopy (EDX) in the same region.

post-mortem cross section image of the degraded LSC cell. The thickness of the LSC electrode is $12 \mu\text{m}$ ($\pm 0.5 \mu\text{m}$) and the porosity 33%. The average particle sizes of the grains within the LSC electrode are between 0.25 and 0.5 μm . At the LSC/GDC interface, severe delamination of the electrode is observed (Figure 8), which is a common failure mode in SOECs [15, 17, 46] and explains the degradation of the LSC cell during the long-term test (Figure 4). In addition, the EDX elemental map for Sr shown in Figure 8c indicates that Sr is enriched (compared to the bulk of the LSC electrode) in the near-surface region – as well as at the LSC/GDC and GDC/YSZ interfaces. The porosity of the GDC barrier estimated via thresholding is about 12%.

The post-mortem cross-section image of the degraded LPNSSC cell is shown in Figure 9a. The thickness of the LPNSSC electrode is $16 \pm 0.3 \mu\text{m}$ and the porosity is estimated to be 22%. Comparing Figure 6a (fresh LPNSSC cell) and Figure 9a (post-mortem LPNSSC cell), the microstructure of the air electrode after long-term test-

ing is comparable to that of the as-prepared electrode in terms of thickness and porosity. The porosity of the GDC barrier of the LPNSSC cell is relatively high with 23% and thus SrZrO_3 (refer to Sr- and Zr-maps in Figure 9) is found at the YSZ/GDC interface, formed by cation interdiffusion between the air electrode and electrolyte through the barrier layer. Since SrZrO_3 formation usually occurs during sintering of the air electrode at elevated temperatures [45], these effects are ascribed mainly to pre-test processing and not to long-term degradation during cell testing at 800°C .

Figure 10a,b illustrates post-mortem surface FESEM images of the LSC electrode. In addition to the LSC grains, angular particles are observed, which appear in a darker contrast in the BSE image. Similar particles are also found in the post-mortem analysis of the LPNSSC surface (Figure 10c,d). According to the EDX elemental maps of the LPNSSC and LSC surfaces in Figures S9 and S10, these particles are composed of Sr, S and O, indicating the formation of SrSO_4 , which is coupled to phase decomposition

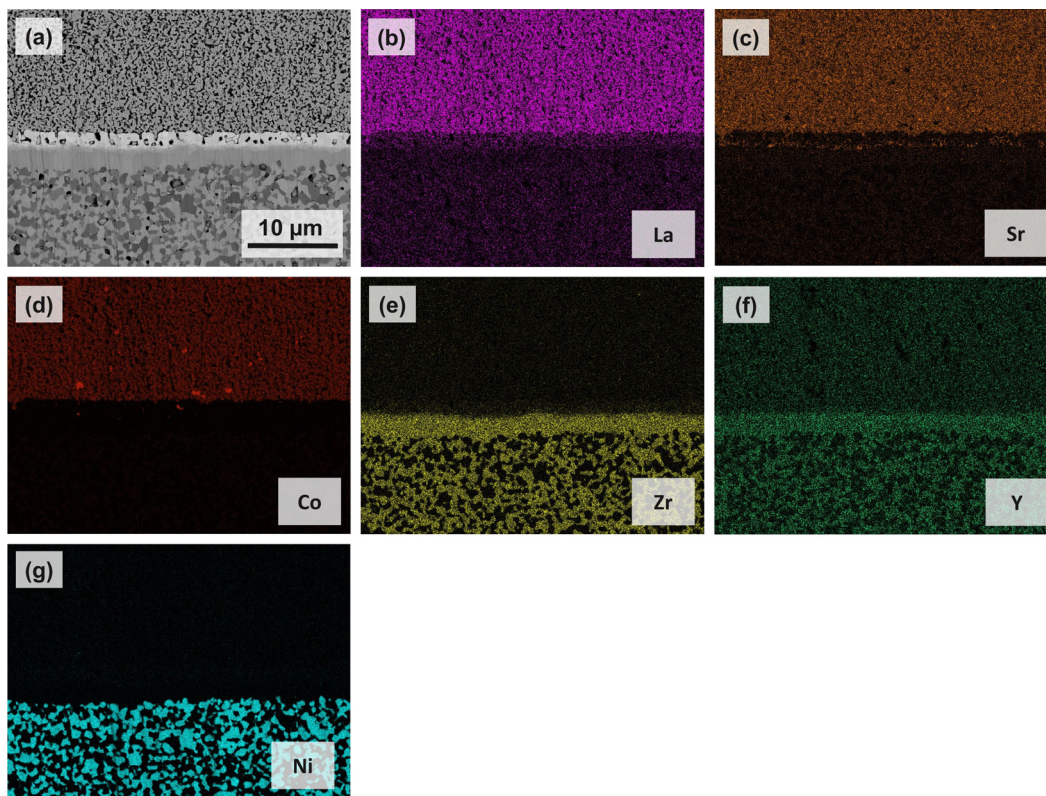


FIGURE 7 Cross-section image of a fresh $5 \times 5 \text{ cm}^2$ anode-supported cell (ASC) with $\text{La}_{0.6}\text{Sr}_{0.4}\text{CoO}_{3-\delta}$ (LSC) air electrode recorded by (a) FESEM-BSE; (b–g) elemental maps for La, Sr, Co, Zr, Y, and Ni acquired by energy dispersive X-ray spectroscopy (EDX) in the same region.

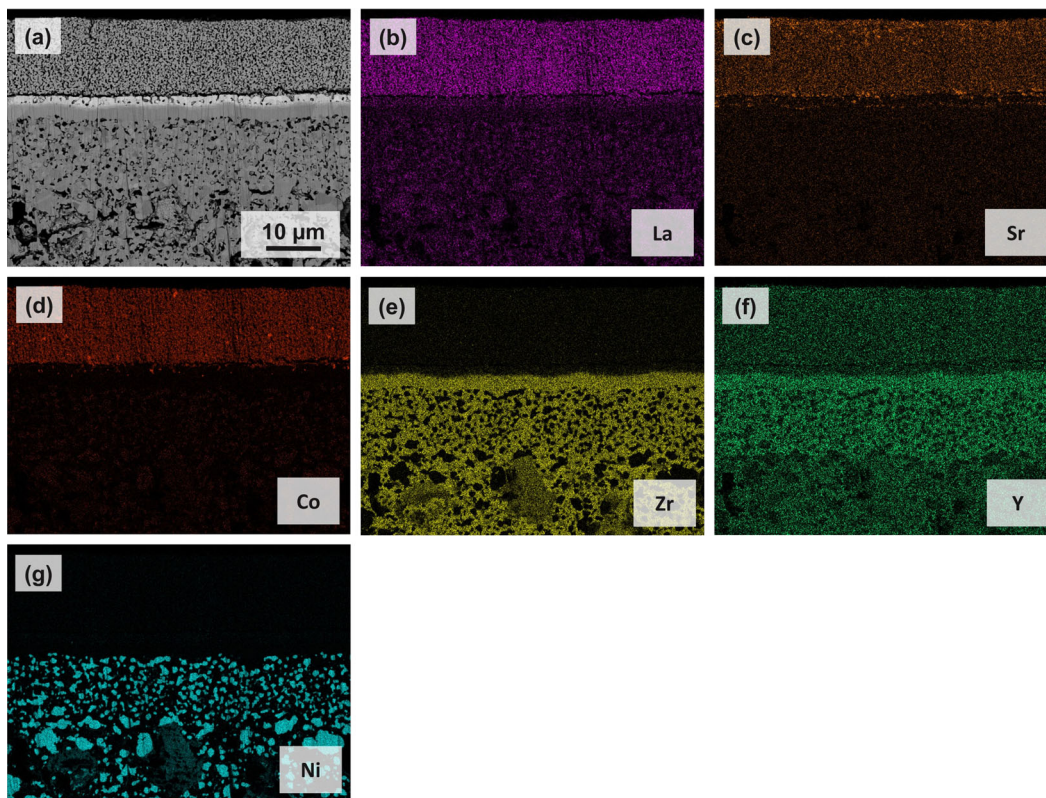


FIGURE 8 Post-mortem cross-section image of a $5 \times 5 \text{ cm}^2$ anode-supported cell (ASC) with $\text{La}_{0.6}\text{Sr}_{0.4}\text{CoO}_{3-\delta}$ (LSC) air electrode obtained by (a) FESEM-BSE after long-term polarization in solid oxide electrolysis cell (SOEC) mode; (b–g) elemental maps for La, Sr, Co, Zr, Y, and Ni acquired by energy dispersive X-ray spectroscopy (EDX) in the same sample region.

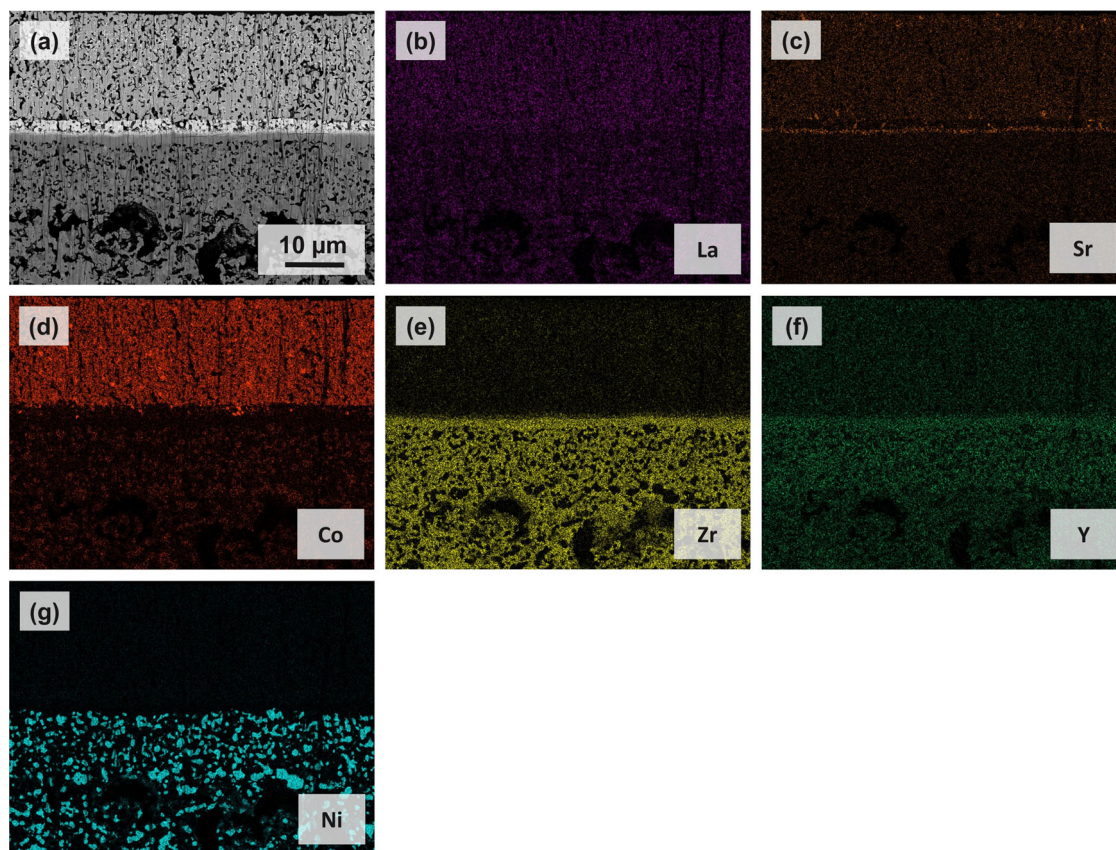


FIGURE 9 Post-mortem cross-section image of a $5 \times 5 \text{ cm}^2$ anode-supported cell (ASC) with $\text{La}_{0.2}\text{Pr}_{0.2}\text{Nd}_{0.2}\text{Sm}_{0.2}\text{Sr}_{0.2}\text{CoO}_{3-\delta}$ (LPNSSC) air electrode obtained by (a) FESEM-BSE after long-term polarization in solid oxide electrolysis cell (SOEC) mode; (b–g) elemental maps for La, Sr, Co, Zr, Y, and Ni acquired by energy dispersive X-ray spectroscopy (EDX) in the same sample region.

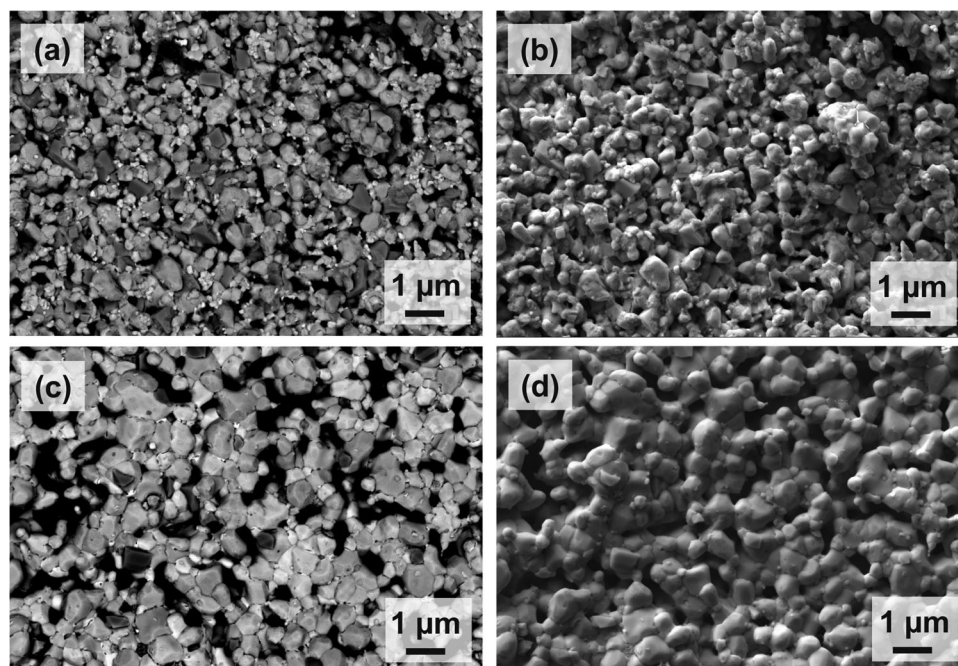


FIGURE 10 Post-mortem microstructure images of the surface of (a, b) the $\text{La}_{0.6}\text{Sr}_{0.4}\text{CoO}_{3-\delta}$ (LSC) air electrode and (c, d) the $\text{La}_{0.2}\text{Pr}_{0.2}\text{Nd}_{0.2}\text{Sm}_{0.2}\text{Sr}_{0.2}\text{CoO}_{3-\delta}$ (LPNSSC) air electrode after long-term polarization of $5 \times 5 \text{ cm}^2$ anode-supported cells (ASCs) in solid oxide electrolysis cell (SOEC) mode; images (a) and (c) were acquired by FESEM-BSE, images (b) and (d) by FESEM-SE.

of the perovskite phase, as previously reported in the literature [47–50]. A comparison of Figure 10a,c shows that the amount of this secondary phase is significantly less on the surface of the degraded LPNSSC electrode (~3% SrSO₄ after 700 h) than on the LSC electrode (~8% SrSO₄ after 400 h). The relative amount of SrSO₄ particles was determined using thresholding-based image analysis, whereby particles in question are distinguished from the bulk using differences in gray values as one criterion. Care was taken to complement the software-based selection by manually including SrSO₄ particles based on their distinctive angular shape.

In addition, the BSE images of both LSC and LPNSSC electrodes (Figure 10a,c) feature small particles, which appear as bright spots. EDX analysis shows that these are Pt particles originating from the Pt paste used for current collection at the air electrode. Post-mortem analyses of the Ni-YSZ fuel electrodes (Figures 8 and 9) show no significant differences between the LSC and LPNSSC cells, confirming that the observed degradation (Figure 4) is mainly due to changes at the air electrodes.

4 | CONCLUSIONS

Solid oxide cells with high-entropy perovskite LPNSSC air electrodes are characterized with regard to electrochemical performance and microstructure. For a planar 5×5 cm² cell, a current density of −1.24 A/cm² is reached in SOEC mode at 1.2 V and 800°C with 90% humidity (rest H₂). This performance surpasses that of a commercial cell with state-of-the-art LSC air electrodes for identical test conditions. Long-term electrolysis during 700 h at 800°C reveals remarkable long-term stability of the LPNSSC cell. Under the same conditions, the voltage of the LSC cell increases continuously for 400 h. According to post-test analyses, the differences in stability during long-term testing can be attributed to the LSC and LPNSSC air electrodes. While delamination of the LSC electrode occurred at the LSC/GDC interface, good adhesion of LPNSSC was observed even after 700 h of electrolysis. The air electrode surfaces of both cells show the formation of secondary phases, especially SrSO₄. However, significantly less SrSO₄ is formed on LPNSSC compared to LSC.


In conclusion, the high-entropy perovskite LPNSSC is a promising option for SOC air electrodes. While LPNSSC cells can compete with – or even surpass – SOTA cells based on LSC with respect to electrochemical performance, they could be especially advantageous regarding long-term stability in SOEC mode. Two of the most critical problems of SOC air electrodes, namely delamination and secondary phase formation due to Sr segregation and SO₂ poisoning, are alleviated compared to SOTA LSC elec-

trodes. Further development of LPNSSC air electrodes is aimed at optimizing the microstructure (e.g., grain sizes, porosity, tortuosity, etc.) to further enhance the electrode performance [51–53]. In addition, the issue of SrZrO₃ formation at the electrolyte-barrier layer interface should be addressed, mainly by decreasing the porosity of the GDC diffusion barrier.

ACKNOWLEDGMENTS

Funding by “Zukunftsfonds Steiermark” within the program “NEXT GREEN TECH – Energy Systems, Green Hydrogen & Green Mobility”, project no. 1704, is gratefully acknowledged. We thank J. Woisik for the FESEM measurements.

ORCID

Patrick Pretschuh  <https://orcid.org/0000-0002-8807-122X>

Andreas Egger  <https://orcid.org/0000-0002-1577-4725>

Edith Bucher  <https://orcid.org/0000-0002-9017-9555>

REFERENCES

1. P. P. Edwards, V. L. Kuznetsov, W. I. F. David, N. P. Brandon, *Energy Policy* **2008**, *36*, 4356.
2. N. Z. Muradov, T. N. Veziroğlu, *Int. J. Hydrogen Energy* **2008**, *33*, 6804.
3. Y. Zhou, R. Li, Z. Lv, J. Liu, H. Zhou, C. Xu, *Chin. J. Chem. Eng.* **2022**, *43*, 2.
4. I. P. Jain, *Int. J. Hydrogen Energy* **2009**, *34*, 7368.
5. R. Shinnar, *Technol. Soc.* **2003**, *25*, 455.
6. K. C. Sabat, A. B. Murphy, *Metall. Mater. Trans. B* **2017**, *48*, 1561.
7. O. Posdziech, T. Geißler, K. Schwarze, R. Blumentritt, *ECS Trans.* **2019**, *91*, 2537.
8. C. Lenser, D. Udomsilp, N. Menzler, P. Holtappels, T. Fujisaki, K. Leonard, H. Matsumoto, A. Sabato, F. Smeacetto, A. Chrysanthou, S. Molin, *Advanced Ceramics for Energy Conversion and Storage* In (Eds: O. Guillon), Elsevier, **2019**, p. 387. <https://doi.org/10.1016/B978-0-08-102726-4.00009-0>
9. S. Y. Gómez, D. Hotza, *Renew. Sustain. Energy Rev.* **2016**, *61*, 155.
10. K. Motylinski, J. Kupecki, B. Numan, Y. S. Hajimolana, V. Venkataraman, *Energy Conver. Manag.* **2021**, *228*, 113674.
11. F. Wang, L. Wang, Y. Ou, X. Lei, J. Yuan, X. Liu, Y. Zhu, *Case Stud. Thermal Eng.* **2021**, *27*, 101240.
12. O. Schmidt, A. Gambhir, I. Staffell, A. Hawkes, J. Nelson, S. Few, *Int. J. Hydrogen Energy* **2017**, *42*, 30470.
13. M. S. Khan, X. Xu, R. Knibbe, Z. Zhu, *Renew. Sustain. Energy Rev.* **2021**, *143*, 110918.
14. Y. Wang, W. Li, L. Ma, W. Li, X. Liu, *Journal of Mater. Sci. Technol.* **2020**, *55*, 35.
15. I. Sreedhar, B. Agarwal, P. Goyal, A. Agarwal, *J. Solid State Electrochem.* **2020**, *24*, 1239.
16. P. Moçoteguy, A. Brisse, *Int. J. Hydrogen Energy* **2013**, *38*, 15887.
17. A. V. Virkar, *Int. J. Hydrogen Energy* **2010**, *35*, 9527.
18. L. C. Baqué, A. L. Soldati, E. Teixeira-Neto, H. E. Troiani, A. Schreiber, A. C. Serquis, *J. Power Sources* **2017**, *337*, 166.

19. K. Develos-Bagarinao, J. De Vero, H. Kishimoto, T. Ishiyama, K. Yamaji, T. Horita, H. Yokokawa, *Phys. Chem. Chem. Phys.* **2019**, *21*, 7183.
20. E. Ostrovskiy, Y.-L. Huang, E. D. Wachsman, *J. Mater. Chem. A* **2021**, *9*, 1593.
21. S. P. Simner, M. D. Anderson, M. H. Engelhard, J. W. Stevenson, *Electrochem. Solid State Lett.* **2006**, *9*, A478.
22. K. Chen, S. P. Jiang, *Electrochem. Energy Rev.* **2020**, *3*, 730.
23. G. M. Rupp, H. T  llez, J. Druce, A. Limbeck, T. Ishihara, J. Kilner, J. Fleig, *J. Mater. Chem. A* **2015**, *3*, 22759.
24. A. K. Opitz, C. Rameshan, M. Kubicek, G. M. Rupp, A. Nanning, T. G  tsch, R. Blume, M. H  vecker, A. Knop-Gericke, G. Rupprechter, B. Kl  tzer, J. Fleig, *Topics Catal.* **2018**, *61*, 2129.
25. N. K. Patel, R. G. Utter, D. Das, M. Pecht, *J. Power Sources* **2019**, *438*, 227040.
26. M. A. R. Niania, A. K. Rossall, J. A. Van den Berg, J. A. Kilner, *J. Mater. Chem. A* **2020**, *8*, 19414.
27. C. M. Rost, E. Sacht, T. Borman, A. Moballegh, E. C. Dickey, D. Hou, J. L. Jones, S. Curtarolo, J.-P. Maria, *Nat. Commun.* **2015**, *6*, 8485.
28. P. A. Krawczyk, M. Jurczyszyn, J. Pawlak, W. Salamon, P. Baran, A. Kmita,  . Gondek, M. Sikora, C. Kapusta, T. Str  czek, J. Wyrwa, A.  ywczyak, *ACS Appl. Electr. Mater.* **2020**, *2*, 3211.
29. S. Jiang, T. Hu, J. Gild, N. Zhou, J. Nie, M. Qin, T. Harrington, K. Vecchio, J. Luo, *Scripta Materialia* **2018**, *142*, 116.
30. A. Sarkar, Q. Wang, A. Schiele, M. R. Chellali, S. S. Bhattacharya, D. Wang, T. Brezesinski, H. Hahn, L. Velasco, B. Breitung, *Adv. Mater.* **2019**, *31*, 1806236.
31. L. Shen, Z. Du, Y. Zhang, X. Dong, H. Zhao, *Appl. Catal. B Environ.* **2021**, *295*, 120264.
32. Y. Yang, H. Bao, H. Ni, X. Ou, S. Wang, B. Lin, P. Feng, Y. Ling, *J. Power Sources* **2021**, *482*, 228959.
33. Q. Yang, G. Wang, H. Wu, B. A. Beshiwork, D. Tian, S. Zhu, Y. Yang, X. Lu, Y. Ding, Y. Ling, Y. Chen, B. Lin, *J. Alloys Compounds* **2021**, *872*, 159633.
34. J. D  browa, A. Olszewska, A. Falkenstein, C. Schwab, M. Szymczak, M. Zajusz, M. Mo  dzierz, A. Miku  a, K. Zieli  nska, K. Berent, T. Czeppe, M. Martin, K.  wierczek, *J. Mater. Chem. A* **2020**, *8*, 24455.
35. A. N. Petrov, O. F. Kononchuk, A. V. Andreev, V. A. Cherepanov, P. K. Kofstad, *Solid State Ionics* **1995**, *80*, 189.
36. A. Egger, E. Bucher, M. Yang, W. Sitte, *Solid State Ionics* **2012**, *225*, 55.
37. A. Egger, M. Perz, E. Bucher, C. Gspan, W. Sitte, *Fuel Cells* **2019**, *19*, 458.
38. P. Hjalmarsson, M. S  gaard, M. Mogensen, *Solid State Ionics* **2008**, *179*, 1422.
39. R. Shannon, *Acta Crystallographica Sect. A* **1976**, *32*, 751.
40. J. Fleig, *Solid State Ionics* **2002**, *150*, 181.
41. B. K  nigshofer, M. H  ber, G. Nusev, P. Bo  koski, C. Hochenauer, V. Subotić, *J. Power Sources* **2022**, *523*, 230982.
42. X. Sun, P. V. Hendriksen, M. B. Mogensen, M. Chen, *Fuel Cells* **2019**, *19*, 740.
43. T. L. Skaft  , O. B. Rizvandi, A. L. Smitshuysen, H. L. Frandsen, J. V. Thorvald H  gh, A. Hauch, S. K. K  r, S. S. Araya, C. Graves, M. B. Mogensen, S. H. Jensen, *J. Power Sources* **2022**, *523*, 231040.
44. C. A. Schneider, W. S. Rasband, K. W. Eliceiri, *Nat. Methods* **2012**, *9*, 671.
45. J. Sz  sz, F. Wankm  ller, V. Wilde, H. St  rmer, D. Gerthsen, N. H. Menzler, E. Ivers-Tiff  e, *J. Electrochem. Soc.* **2018**, *165*, F898.
46. Z. Pan, Q. Liu, Z. Yan, Z. Jiao, L. Bi, S. H. Chan, Z. Zhong, *Electrochem. Commun.* **2022**, *137*, 107267.
47. E. Bucher, C. Gspan, F. Hofer, W. Sitte, *Solid State Ionics* **2013**, *238*, 15.
48. E. Bucher, C. Gspan, W. Sitte, *Solid State Ionics* **2015**, *272*, 112.
49. H. Yokokawa, N. Sakai, T. Horita, K. Yamaji, (Eds.), *Handbook of Fuel Cells*, John Wiley & Sons, Ltd., Hoboken **2009**. p. 979.
50. F. Wang, H. Kishimoto, T. Ishiyama, K. Develos-Bagarinao, K. Yamaji, T. Horita, H. Yokokawa, *J. Power Sources* **2020**, *478*, 228763.
51. M. Laguna-Bercero, R. Campana,  . Larrea, J. A. Kilner, V. M. Orera, *J. Power Sources* **2011**, *196*, 8942.
52. S. Kim, D. W. Joh, D.-Y. Lee, J. Lee, H. S. Kim, M. Z. Khan, J. E. Hong, S.-B. Lee, S. J. Park, R.-H. Song, M. T. Mehran, C. K. Rhee, T.-H. Lim, *Chem. Eng. J.* **2021**, *410*, 128318.
53. W. Li, Y. Shi, Y. Luo, N. Cai, *Int. J. Hydrogen Energy* **2014**, *39*, 13738.

SUPPORTING INFORMATION

Additional supporting information can be found online in the Supporting Information section at the end of this article.

How to cite this article: P. Pretschuh, A. Egger, R. Brunner, E. Bucher, *Fuel Cells* **2023**, *1*.
<https://doi.org/10.1002/face.202300036>